Title
Insights into Copper Sulfide Formation from Cu and S K edge XAS and DFT studies

Journal
Inorganic Chemistry, 59(20)

ISSN
0020-1669

Authors
Azzam, Sara A
Boubnov, Alexey
Hoffman, Adam S
et al.

Publication Date
2020-10-19

DOI
10.1021/acs.inorgchem.0c02232

Insights into Copper Sulfide Formation from Cu and S K-edge XAS and DFT studies

Sara A. Azzam[1], Alexey Boubnov[2§], Adam S. Hoffman[2], Tirso López-Ausens[1], Nicole Chiang[1], Griffin Canning[3], Philippe Sautet[1,4], Simon R. Bare[2] and Dante A. Simonetti[1,5*]*

[1]Chemical and Biomolecular Engineering Department, University of California Los Angeles, Los Angeles, CA 90095

[2]Stanford Synchrotron Radiation Lightsource, SLAC National Accelerator Laboratory, Menlo Park, CA 94025

[3]Department of Chemistry and Chemical Biology, University of New Mexico, Albuquerque, NM 57131

[4]Department of Chemistry and Biochemistry, University of California Los Angeles, Los Angeles, CA, USA, 90024

[5]Institute for Carbon Management (ICM), 420 Westwood Plaza, Los Angeles, California 90095

[§]Present address: Institute for Chemical Technology and Polymer Chemistry, Karlsruhe Institute of Technology, 76131 Karlsruhe, Germany

[*]Corresponding authors: Email: dasimonetti@ucla.edu
Email: srbare@slac.stanford.edu

ABSTRACT Understanding the fundamentals of the reaction between CuO with trace amounts of H_2S to form CuS products is critical for the optimal utilization of this process in sulfur removal applications. Unfortunately, CuS is a complex material, featuring various $Cu_{2-x}S$ compounds (with $0 \leq x \leq 1$), distorted crystal phases, and varying electronic structures and coordination environments of Cu and S ions. In this work, we combine *ex-situ* and *in-situ* X-ray absorption spectroscopy (XAS) at S and Cu K-edges, fixed bed sorption experiments, DFT simulations, and other characterization techniques to speciate the CuS products formed at different temperatures (298-383 K) and from CuO sorbents with different crystallite sizes (2.8-40 nm). The results of our analysis identify the formation of a distorted CuS layer at the surface of CuO crystals with disulfide groups with longer Cu-S bonds and higher delocalization of the positive charge of the Cu center into $(S^{-1})_2$. This distorted CuS layer dominates the XAS signal at lower temperatures (298-323 K) and at the initial stages of sulfidation at higher temperatures (353 K and 383 K) where conversion is low (<40%). First principles atomistic simulations confirm the thermodynamic favorability of the formation of surface $(S^{-1})_2$ on both CuO (111) and $(\bar{1}11)$ surfaces, providing further support for our experimental observations. Furthermore, these simulations reveal that the presence of disulfide bonds stabilize surface hydroxyl groups, leading to lower Gibbs Free Energies of their surface migration.

Keywords: Copper oxide, desulfurization, reactive sorption, X-ray absorption spectrometry

1. Introduction

Hydrocarbon streams derived from natural gas and petroleum processing contain high concentrations of hydrogen sulfide (H_2S) which is corrosive to process equipment, detrimental to product quality, and harmful to the environment.[1–3] Therefore, purification of these streams to sub-ppm concentrations of H_2S is required, and a chemical reaction using a metal oxide is often employed to achieve these low concentrations because of favorable reaction thermodynamics and permanent sequestration of H_2S as a solid metal sulfide.[4,5] Reaction of copper oxide (CuO) with H_2S to form water and copper sulfide is an effective process for reactive sorption because complete conversion of CuO (and ppb levels of H_2S) can be achieved at ambient conditions.[6,7] However, the removal capacities of CuO sorbents vary widely even between materials with apparently similar chemical and structural properties.[6] Indeed, an understanding of molecular level details of the reaction is imperative for uncovering the source of this variability and developing reliable CuO sorbents for this process.

Earlier work has demonstrated the critical role of crystallite size and micro-porosity in predicting the performance of CuO sorbents at both fixed bed and individual micrometer-sized particle scales.[7] The synchrotron-based techniques of X-ray absorption spectroscopy (XAS) and transmission X-ray microscopy (TXM) have been successfully used to quantify the kinetics of the sulfidation process and to observe the chemical and structural changes that are associated with it in real time. These studies confirmed the presence of pore diffusion resistance within individual particles (< 10 μm) and hinted at the potential formation of different copper sulfide products.[6] Additionally, fixed bed experiments and Density Functional Theory (DFT) calculations showed that reducing crystallite size leads to an improvement in the removal capacity of CuO sorbents.[7] This work uncovered a difference in reactivity of oxygen atoms based on their coordination

environment, with three-fold coordinated atoms, more abundant in smaller crystals, being more reactive towards sulfur than four-fold coordinated oxygen. Furthermore, these three-fold coordinated oxygen atoms form oxygen vacancies more readily, which could indicate more facile diffusion of atoms through the bulk of the solid phase in smaller crystals. These studies introduced new questions pertaining the reaction of CuO with H_2S, such as what the type of copper sulfide species are formed, do these phases depend on the structure of the starting material or/and the conditions of the sulfidation process, and how does the phase formation impact the final conversion (and thus, performance) of the material.

The conventional stoichiometry used for the CuO sulfidation reaction assumes the formation of covellite (CuS), however, new emerging evidence has challenged this long-held belief of the formation of a single product species/phase.[6] Indeed, copper sulfide systems are highly complex, featuring a range of species with $Cu_{2-x}S$ stoichiometries ($0 \leq x \leq 1$), diverse crystal phases, and varying bonding arrangements and electronic structures (discussed subsequently).[8–10] The crystallographic characterization of these intermediate $Cu_{2-x}S$ species (between Cu_2S and CuS) is difficult due to the ill-defined positions of the copper atoms within the close-packed sublattice of S atoms. Despite their simple chemical formulae, the two end members (i.e., $x = 0$ or 1) of the $Cu_{2-x}S$ family, Cu_2S (chalcocite) and CuS (covellite), also have complex crystalline structures. Covellite features a hexagonal crystalline structure, with two thirds of the Cu atoms in tetrahedral coordination and the other third has a trigonal planar symmetry; the oxidation states of Cu in these centers are +1 and +2, respectively. On the other hand, one-third of S atoms are monosulfides (S^{2-}) in trigonal bi-pyramidal coordination, and two thirds are in disulfide (S^{1-}-S^{-1}) arrangement. These atoms are arranged in alternating S_2 and CuS_3-CuS_3 layers as shown in **Figure S1**. Chalcocite (Cu_2S) is known for its instability and its inclination to degrade to copper deficient species at

ambient conditions. The oxidation state of Cu in the 96-atom monoclinic unit of chalcocite is mostly +1 with evidence of mobile Cu (0) centers.[11] Successful elucidation of copper sulfide species that form (and evolve) during reactions between CuO and H_2S will fill a gap in the efforts towards fundamental understanding of this reaction, and the evident complexity of copper sulfides calls for the use of advanced characterization techniques that can probe the oxidation states, local geometry, bond lengths and coordination numbers of both Cu and S in order to achieve accurate speciation.

XAS is a powerful technique that can provide valuable information in this regard, by both *ex-situ* analysis of fresh and spent samples and *in-situ* study of the evolved species throughout the course of the reaction.[12,13] The extended X-ray absorption fine structure (EXAFS) can be used to determine local structural information about the target atom, and the near-edge structure can provide information about the oxidation state of an atom and its coordination symmetry.[12,13] Nevertheless, probing a heterogeneous mixture of species, such as a partially sulfided CuO sample, is a challenging task because of the numerous local environments of Cu within one phase (CuS) and across the two phases (CuO and CuS). In this work, we probe the reaction of CuO with dilute H_2S gas streams (1000 ppm-vol in He or N_2) using *in-situ* and *ex-situ* XAS at both the S K- and Cu K-edges. We verify that *in-situ* XAS experiments accurately represent this reactions by comparison with the capacities and kinetics from fixed bed absorption studies at the same conditions. These experimental techniques (and the resulting data) are also used to probe the influence of CuO crystallite sizes (across a range of 2 – 40 nm) and reaction temperature (298-383 K) on $Cu_{2-x}S$ formation. The results of our work suggest the formation of a distorted CuS layer at the surface of the CuO crystals, with disulfide groups of longer Cu-S bonds and higher delocalization of the positive charge of Cu center into $(S^{-1})_2$ at the initial stages of the reaction. Our

findings also suggest the dominance of these species at lower temperatures (298-323 K) compared to higher temperatures (353-383 K) and where the CuS products more closely resemble pure covellite. DFT calculations for the sulfidation of CuO (111) and ($\bar{1}$11) surfaces also support our hypothesis of the formation and dominance of disulfides at the initial stages of CuO sulfidation.

2. Experimental Methods

2.1 Materials

A commercial CuO-based sorbent (HiFUEL W230; denoted as **CuO-1**) was purchased from Alfa Aesar and tested without subsequent treatment. This sorbent is composed of 63.5 wt% CuO, 25 wt% ZnO, and 10 wt% Al_2O_3. For the synthesis of all other CuO sorbents, copper (II) nitrate trihydrate (Sigma Aldrich, 99%), copper (II) acetate monohydrate (Sigma Aldrich, 99%), sodium hydroxide (BDH, 97%) and glacial acetic acid (VWR, ACS grade) were used in the preparation.

CuO nanoparticles (denoted as **CuO-2** and **CuO-3**) were prepared using an acid-catalyzed sol-gel process.[14] For CuO-2, 1.0 cm^3 of glacial acetic acid was added to 300 cm^3 of 0.02 M copper (II) acetate solution under vigorous stirring and heating. Upon boiling, 0.8 g of sodium hydroxide was added to the solution under continuous stirring. The solution was then allowed to cool to room temperature while a black solid continuously precipitated out of solution. The solid precipitate was recovered via centrifugation of the solution for 10 minutes (JA-14 rotor) at 293 K and 6000 RPM followed by decanting the supernatant liquid. The precipitate was then washed with deionized water and ethanol. The washed precipitate was dried in a furnace for 8 h at 313 K. Sample CuO-3 was prepared by additional thermal treatment of sample CuO-2 in air at 623 K for 4 hours to achieve larger crystallite size (as evidenced by X-ray diffraction patterns). Additional CuO nanoparticles (denoted as **CuO-4**) were prepared by a drop-wise addition of aqueous 0.1 M sodium hydroxide solution to aqueous 0.1 M copper (II) nitrate trihydrate solution under continuous

mixing. The obtained material, copper (II) hydroxide, was then vacuum filtered and washed with distilled water and ethanol, dried in air at 353 K for 14 h, and then thermally treated in air at 773 K for 4 h at a ramping rate of 1 K h^{-1}.

CuO nanofibers (denoted as **CuO-5**) were synthesized through electrospinning. Polymer solutions were prepared by dissolving 1.30 g of PVP M.W. 1,300,000 in ethanol solvent (23 cm^3). The polymer solution was then vortexed (Fisher Scientific Digital Vortex Mixer) at 3000 rpm for 1 h until the polymer was completely dissolved. The solution was left to settle for 10 minutes, transferred to a beaker, and stirred for 0.5 h. The metal containing solution was prepared by dissolving copper (II) nitrate (1.3 g) in 10 cm^3 of DI water and stirring the solution for 0.5 h. The copper containing solution was then added dropwise to the polymer containing solution. The solution was stirred for 0.25 h, and then vortexed for 0.5 h at 3000 rpm. The electrospinning solution was placed in a 10 mL syringe (BD 10 mL syringe with Luer Lok™ tip) with a hypodermic needle (Monoject™ Standard 30G x ¾"). The distance between the tip of the needle and a stainless-steel collecting plate, which was covered with aluminum foil, was 22 inches. A Gamma High Voltage Research ES75 power supply was used to apply 30 kV on the polymer jet while the polymer solution was extruded through the needle at a rate controlled by a syringe pump (1.0 cm^3 h^{-1}; Kent Scientific Genie Plus). Dry air was circulated inside a 3 m^3 chamber at 6 cm^3 min^{-1} to control the relative humidity at 19.5 ± 2%. The collected fibers were thermally treated in air at 823 K for 4 h at a ramping rate of 2.0 K min^{-1} to remove the majority of PVP and form CuO.

2.2 Non-synchrotron characterization techniques

All CuO sorbents were characterized using a variety of techniques. Powder X-ray diffraction patterns were obtained on an X-ray diffractometer (JEOL JDX-3530 and Philips X-Pert) using Cu Kα radiation of 1.5410 Å wavelength and used to identify the crystalline copper-containing phases.

The average crystallite size of each sample was determined using Scherrer's formula. Nitrogen adsorption-desorption isotherms were measured at 77 K with a Micromeritics ASAP 2020 Plus system. Before measurements, the samples were degassed at 1×10^{-3} Torr and 573 K. The Brunauer-Emmett-Teller (BET) surface areas were calculated from the isotherms. The pore size distribution was derived from the adsorption branches of the isotherms using the Barrett-Joyner-Halenda (BJH) model. Scanning electron microscopy (NOVA 230 Nano SEM) was used to visualize the morphology of the materials. The diameters of the agglomerate sizes of the sorbents were measured from the SEM images using ImageJ software.

2.3. Fixed bed sulfidation tests

Fixed-bed sorption breakthrough experiments were carried out in the apparatus outlined in **Figure S2**. A tubular stainless-steel reactor with 0.25-inch outer diameter was packed with 100-180 mg of sorbents with average agglomerate sizes of 75 µm (i.e., particles sieved through +200-100 mesh screens). The packed beds were 1.5 cm in height and were fixed between two plugs of quartz wool. The temperature of the reactor (298-383 K) was regulated using a resistively heated jacket with a PID temperature controller (TEMPCO EPC-100). Reactant feed streams consisted of 1000 ppm-vol H_2S in N_2 and were produced by diluting 1.0% H_2S/N_2 (Praxair) in UHP N_2. The total inlet flowrate of 90 cm^3(STP) min^{-1} was controlled using MKS GE50A and GM50A flow controllers. Online gas chromatography (Agilent 7890B) with a sulfur chemiluminescence detector (SCD; Agilent 755) was used to measure the concentration of H_2S in inlet and outlet streams. The interior of the reactor and all the gas transfer lines were treated by an inert coating (SilcoNert 2000) to mitigate adsorption of sulfur onto the walls of the apparatus tubing.

2.4 XAS acquisition and analysis

S K- and Cu K-edge X-ray absorption spectra were recorded at Stanford Synchrotron Radiation Lightsource (SSRL, California, USA) at wiggler beamline 4-3 using a Si (111) double-crystal monochromator. The storage ring was operated at 3 GeV with a ring current of 494-500 mA in top-up mode. The beam cross-section was 1 mm x 3 mm. X-ray absorption near-edge structure (XANES) spectra were recorded at the S K-edge (2472.0 eV) in fluorescence mode using a 7-element silicon-drift detector (Canberra). Energy calibration was achieved using sodium thiosulfate ($Na_2S_2O_3.5H_2O$) where the first peak of the spectrum was fixed at 2472.0 eV. EXAFS spectra were recorded at the Cu K-edge (8979.0 eV) in transmission mode. A Cu foil, situated between two ionization chambers after the sample, was scanned simultaneously for energy calibration purposes.

The XAS samples comprised a wafer (36 mg of CuO-based sample mixed with 14 mg of boron nitride (BN) (Sigma Aldrich)) for the S K-edge, and 2.4 mg of sample diluted with 47.6 mg BN for the Cu K-edge. The wafer was placed at 45° to the incident beam on a heated stage inside a 100 cm^3 cell, as described previously and as shown in **Figure S3**.[15]

For in-situ XAS sulfidation experiments, 1000 ppm H_2S in Helium (Airgas) and Helium (99.95%, Airgas) gases were used. XAS scans were initially taken under Helium flow, then the temperature was ramped up to the desired set point (298, 323, 353, or 383 K) at a rate of 5 K min^{-1} and under a 20 cm^3(STP) min^{-1} flow of Helium. Once temperature stabilized, XAS scans were taken again to obtain initial spectra at the reaction temperature. After collection of initial spectra, a stream of 1000 ppm H_2S/He was introduced into the reaction cell, and XAS scans were collected continuously (every 6.25 minutes for Cu K-edge and every 5-11 minutes at S K-edge) until saturation was reached. The cell was then purged with Helium at 20 cm^3(STP) min^{-1} and allowed

to cool to room temperature before XAS scans of spent samples were obtained. For the S K-edge, additional XAS scans were obtained for an inert BN sample under H_2S gas flow, in order to allow subtraction of the gas phase H_2S signal contribution from the overall *in-situ* XANES scans.

XAS data were analysed using ATHENA and ARTEMIS from the Demeter package software.[16] The Cu K-edge EXAFS data was extracted from 3.0-11.3 $Å^{-1}$ in *k*-space, and the Fourier transformed data was analyzed in the range of 1.0-2.4 Å for partially sulfided materials and 1.0-3.4 Å for fresh and reference materials. Experimental data were fitted with theoretical back-scattering paths calculated using FEFF6, based upon CIF files from the Inorganic Crystal Structure Database (ICSD).[17] The fits were performed based on k^1, k^2, and k^3 weighting. The amplitude reduction factor, S_0^2, was determined by fitting a reference copper foil, from each beamline visit, with tabulated coordination numbers of bulk copper (*fcc*-Cu metal: ICSD 53247).[17] The average value of S_0^2 value was 0.91 with a standard deviation of 0.05.

Intensity and phase of scattering paths of the oxide materials were calculated using FEFF6 based on crystallographic data from the tenorite CuO structure (ICSD 16025).[17] To simplify the models, only single scattering paths were included and the coordination numbers, N, were scaled by a factor α. The term, α, was introduced in order to account for the size effect on the EXAFS scattering path intensity. This term is a scaling factor for all the scattering paths associated with a spectrum that is consistent across samples of a given crystallite size. The α term is not to be confused with the scaling factor used to account for lattice expansion of cubic systems. The complexities of EXAFS modeling CuO are further discussed in section 3.3 of the Supporting Information.

The intensity and phase of the scattering paths in the sulfided material were also calculated using FEFF6 based on a modified CuS covellite CIF file (ICSD 32105).[17] This modified structure

averages the two Cu centers (tetrahedral Cu^{1+}, and trigonal planar Cu^{2+}) sites in covellite. **Figure 1** presents a stick plot of the averaged coordination numbers and distances for Cu in the modified structure. For a reliable quantification of each of the phases, the fitting model of partially sulfided materials was simplified to take into account only the most significant scattering paths. Because the focus of the EXAFS investigation of these materials was the determination of the types of sulfur species formed, only the first Cu-O and Cu-S shells were fit. In these fits, we assumed that the unreacted CuO material was not significantly modified by the sulfidation reaction. This allowed us to fix the Cu-O path length and associated mean squared displacement term (σ^2) at the values obtained for the starting material, while scaling the coordination number down from the initial value by multiplying with the molar fraction of unreacted material, X_{CuO}. The X_{CuO} term is defined as 1- X_{CuS} where X_{CuS} is the conversion determined by linear combination fitting of the XANES region of sulfided samples. Thus, the CuO component of the final material has fixed EXAFS parameters while the EXAFS parameters of the CuS portion were allowed to vary. These parameters were Cu-S coordination number, *N*, scattering path length, *R,* and its associated mean squared displacement term, σ^2. In all of the fits, ΔE_0 was allowed to vary.

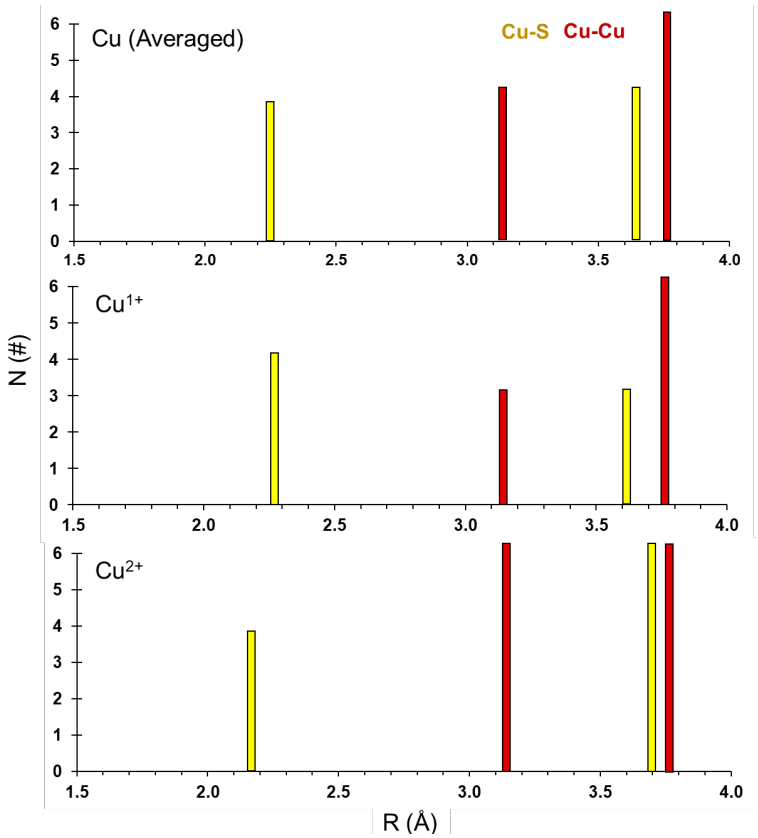

Figure 1. Stick-plot representation of the radial distribution of atoms around Cu^{1+} and Cu^{2+} in CuS (covellite) and averaged Cu center in the simplified CuS model used in EXAFS fitting of Cu K-edge spectra.

2.5 DFT computational study

First principles atomic simulations were conducted using Density Functional Theory as implemented in the quantum mechanical software package VASP with a plane-wave basis set.[18–20] The basis set had an energy cutoff of 400 eV. Exchange and correlation were accounted for with the generalized gradient approximation (GGA),[21] using the Perdew–Burke–Ernzerhof (PBE) functional.[22] Since CuO has an antiferromagnetic ground state, spin polarization was considered for all cases. To this regard, it is known that due to the strong correlation effect among Cu 3*d* electrons in CuO, conventional DFT calculations are unable to properly describe the electronic structure.[22]

In order to account for strong correlation effects, the so-called Hubbard correction[23–25] was used, specifically the GGA+U method as formulated by Dudarev et al..[26] A U_{eff} value of +7 eV for Cu 3*d* electrons was chosen ($U_{eff} = U - J$, with U=7 and J=0 eV), which has previously been found to accurately reproduce experimental properties such as the lattice parameter, band gap and magnetic moment of Cu atoms. [7,27,28] Indeed, the calculated magnetic moment per Cu atom is 0.66 μ_B, in close agreement with the experimental value (0.68 μ_B[29]). Also, for the calculated lattice parameters of bulk CuO we found a = 4.686 Å, b = 3.428 Å, c = 5.122 Å, β = 99.44 and the Cu–O distance to be 1.96 Å, in agreement with experimental measurements.[30]

To study sulfur interaction on these CuO surfaces, a (2 x 1) surface supercell of the (111) and ($\bar{1}$11) surfaces were used. The model for the (111) surface was used to show the thermodynamically favorable formation of S_2 dimers at the molecular level, whereas it is shown in ($\bar{1}$11) surfaces how S-S bonds might affect process involved in the reaction H_2S and CuO. These models are depicted in **Figure 2**.

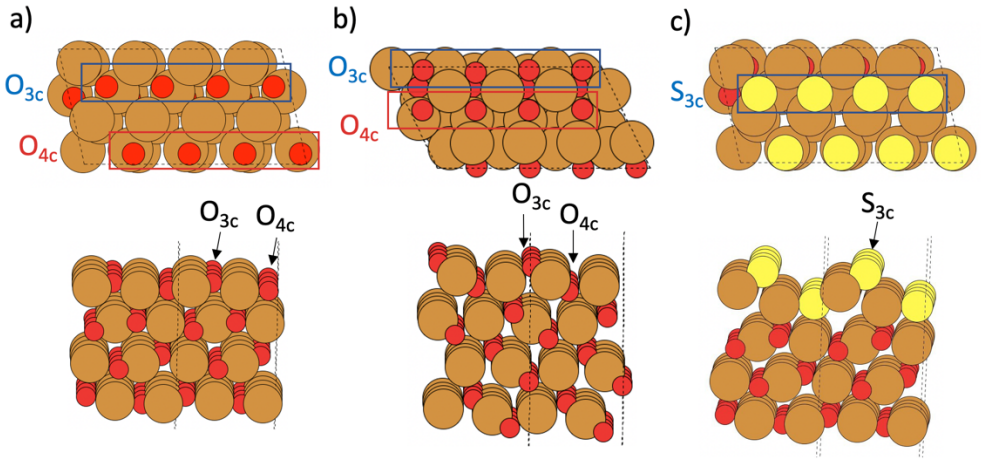

Figure 2. Top view (above) and side view (below) of surface models for a) CuO (111) surface b) CuO ($\bar{1}$11) and c) sulfided CuO (111) considered in this study, showing also 3-fold coordinated oxygen atoms (O_{3c}) and 4-fold ones (O_{4c}). Note that in the side view (below) the unit cells are within dashed lines, with the adjacent one shown for visual purposes.

The CuO (111) and ($\bar{1}$11) surfaces were selected for study as they are the most stable thermodynamic surfaces (surface free energies of 0.75 and 0.89 J m^{-2} respectively)[27] and are experimentally found in CuO materials [7]. Both of them are structurally similar, featuring two types of surface oxygen atoms, namely O_{3c} and O_{4c}. The former is coordinated to three copper atoms, whereas the second one to four copper atoms. They differ notably in reactivity towards H_2S molecules, as will be shown in an upcoming work of our group. O_{3c} centers react first with H_2S molecules than with O_{4c}, giving a partially sulfide surface, from which polysulfide species on the surface can be formed, as it is shown in section 3.4. These surface models were built from the CuO bulk unit cell above described with the ASE software package.[31] The slab thickness was four layers (~8 Å for both surfaces), with a 20 Å vacuum gap between slabs. The Brillouin zone was sampled using a 3x3x1 Monkhorst-Pack[32] *k*-points mesh. A dipole correction was added to avoid spurious inter-slab interaction.[33]

Finally, reaction Gibbs free energies for the surface processes studied computationally were calculated from DFT energies. ΔH for a given process was approximated with DFT energies, i.e.:

$$\Delta G = \Delta H - T\Delta S \approx \Delta E_{DFT} - T\Delta S \quad (1)$$

In section 3.4, when discussing briefly results about net reactions of H_2S with CuO surfaces, we took into account the gaseous entropy of involved molecules, namely H_2S and H_2O. For example, for the adsorption of H_2S over a CuO surface at constant temperature:

$$\Delta G = \Delta H - T\Delta S \approx \Delta E_{DFT} - T\Delta S = \Delta E_{DFT} - T\,[S_{final} - S_{initial}] \quad (2)$$

with $S_{final} = S_{surface+admolecule}$ and $S_{initial} = S_{surface} + S_{molecule}$. Since there is no strong distortion and change of the surface systems we assumed that the change in free energy for the surface was negligible, and hence that $S_{surface} \approx S_{surface+admolecule}$. Therefore, we approximate ΔG in processes involving gaseous H_2S or H_2O as:

$$\Delta G \approx \Delta E_{DFT} + TS_{molecule} \quad (3)$$

However, most of the computational discussion deals with sulfur-sulfur bond formation over CuO surfaces, in which few bonds are formed and broken without changing the coverage or forming new gaseous species. Therefore, we assume entropy is not varied notably in this case and for processes involving the formation polysulfide species we set:

$$S_{final\ step} \approx S_{initial\ step} \quad (4)$$

$$\Delta S = S_{final\ step} - S_{initial\ step} \approx 0 \quad (5)$$

$$\Delta G = \Delta H - T\Delta S \approx \Delta E_{DFT} - T\Delta S \approx \Delta E_{DFT} \quad (6)$$

Note that negative energy values mean a thermodynamically favorable process.

3. Results and Discussion

3.1. Structural characterization of fresh CuO sorbents

Table 1 summarizes the key physical characteristics of the five samples, **CuO-1** – **CuO-5**. The diffraction patterns for all samples, **Figure S4**, show characteristic peaks of single-phase monoclinic CuO. (XRD patterns of sulfided CuO are shown in **Figure S5** and will be discussed in subsequent sections.) The crystallite sizes of the CuO sorbents were determined using Scherrer's formula based on 2θ=38.8°, CuO (111), and are summarized in **Table 1**. The crystallite sizes range from 2.8 nm for CuO-1 to 40 nm for the lab-synthesized nanofibrous sample (CuO-5). The estimated d-spacing for the (200) plane for all samples (2.29-2.30 Å) match literature[12] and confirm the formation of pure monoclinic CuO. The results of N_2-physiosorption experiments are summarized in **Table 1**, and they reveal comparable surface areas (44.5 to 67.3 $m^2\ g^{-1}$) and pore volumes (0.079 to 0.181 $cm^3 g^{-1}$) for all the samples except CuO-5. The notably low surface area and void volume for the nanofiber sample is due to the electrospinning process which produces samples that consist of fibrous networks (nanofibers with diameters between 160-600 nm) with

low meso-porosity, as shown in the SEM images in **Figure S6**. On the other hand, SEM images of the lab-synthesized CuO nanoparticles and CuO-1 sample reveal highly textured micrometer-sized particles consisting of finer agglomerates (<100 nm).

Table 1. Physiochemical properties of the CuO sorbents. [a]Based on XRD peak at 2θ=38.8°. [b]First shell oxygen coordination number based on EXAFS fits of Cu K-edge (See Supporting Information). [c]BET method. [d]BJH method. [e]Fixed bed experiments at 298 K with 90 cm^3(STP) min^{-1} of 1000 vol-ppm H_2S/N_2 at 1 atm total pressure.

Sample ID	Morphology	Crystallite size (nm)[a]	N (Cu-O)[b]	Surface area (m^2g^{-1})[c]	Pore volume (cm^3g^{-1})[d]	Conversion (%)[e]
CuO-1	Nanoparticles	2.8	3.0 ± 1.0	67.3	0.139	44
CuO-2	Nanoparticles	7.0	2.5 ± 1.1	59.1	0.079	28
CuO-3	Nanoparticles	11	3.2 ± 0.4	44.5	0.102	24
CuO-4	Nanoparticles	23	4.0 ± 0.6	58.8	0.181	14
CuO-5	Nanofibers	40	5.4 ± 0.5	7.23	0.006	3

Figure 3 shows the Cu K-edge XANES spectra for the five CuO sorbents. The spectral features for all samples agree qualitatively with a recent XAFS exploration of copper oxide materials.[34] The small pre-edge feature at 8979 eV results from a Cu 1s → $3d^9$ dipole forbidden transition that is completely absent in compounds with the Cu^+ oxidation state due to its fully occupied d shell. This suggests a 2+ oxidation state of Cu in these samples, which is consistent with the electronic structure of Cu in CuO. Moreover, the best-fit model of the Cu K-edge EXAFS data for all the samples contain only scattering paths matching monoclinic CuO (see **Table S1** for a summary of the best fit parameters for the fresh materials). The spectra and fits are displayed in **Figures S7-S11** for fresh CuO samples, and in **Figures S12-S15** for spent samples. Section 3.3 (and **Figures S16-S17**) of the SI provide additional details regarding analysis of CuO EXAFS.

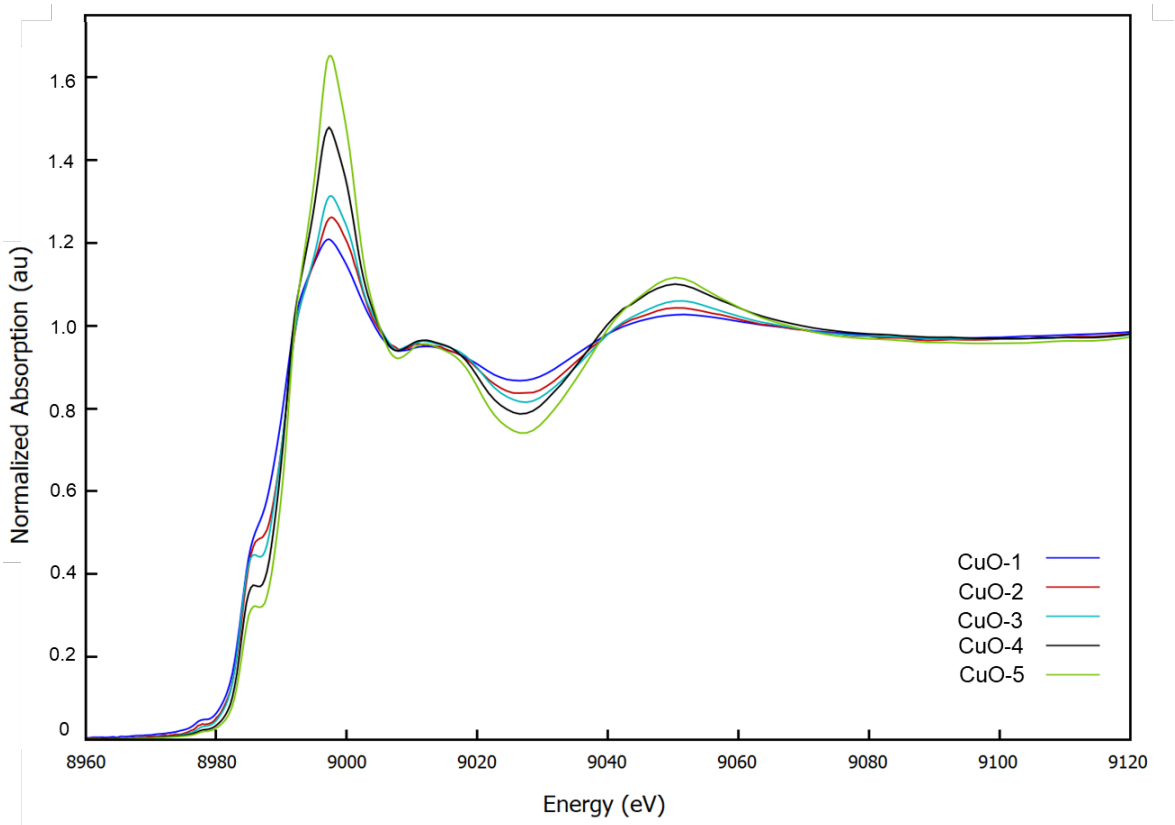

Figure 3. Normalized Cu K-edge XANES spectra for CuO sorbents of different average crystallite sizes: CuO-1 (2.8 nm), CuO-2 (7nm), CuO-3 (11 nm), CuO-4 (23 nm) and CuO-5 (40 nm).

The change in the height of white line in the XANES is consistent with literature, where, in the absence of any chemical change to the material, the height of the white line correlates positively with crystallite size of transition metal oxide systems such as CuO.[35] This amplitude change is also accompanied by a change in the magnitude of the oscillations found in the post edge region of the spectra, i.e. the EXAFS signal. As a result of this change in magnitude, the coordination numbers of each of the constituent scattering paths derived from fitting the EXAFS signal also change. **Table 1** summarizes the coordination numbers of the first shell Cu-O single scattering path as determined by the best-fit model for Cu K-edge EXAFS of the samples. The model-estimated coordination number decreased as crystallite size decreased, with the lowest estimate of 2.5 ± 1.1 in CuO-2 (7 nm) as compared to 5.4 ± 0.5 in CuO-5 (40 nm). **Figure 4** further demonstrates this

relationship between crystallite size and coordination number for the first two oxygen scattering paths. The figure shows clearly an increase in the average coordination number with crystallite size increase (CuO-2 < CuO-3 < CuO-4 < CuO-5) for both scattering paths. Estimating the coordination numbers in fresh samples proved to be essential for fitting the partially sulfided materials. The Cu-S paths were fit to characterize the formed sulfides, while the Cu-O path lengths were fixed to their fresh materials' counterparts, with the necessary conversion adjustment (See section 2.4).

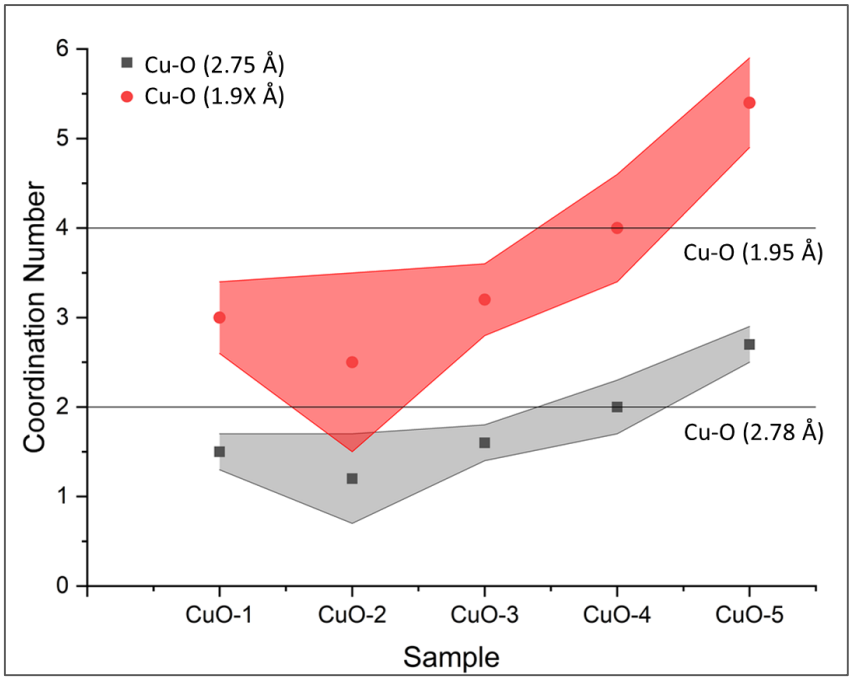

Figure 4. A plot of the coordination numbers of the first two oxygen scattering paths based on the EXAFS fits of the Cu K-edge spectra for the five CuO samples. The horizontal lines represent the bulk coordination numbers of the first two scattering paths in the CuO structure.

3.2 Determination of sorption capacities and kinetics from various techniques

Fixed bed sorption and *in-situ* XAS experiments at Cu and S K-edges were performed to study the sulfidation kinetics of the sample that exhibited the highest conversion, CuO-1, at different temperatures (323 K, 353 K, and 383 K). The effect of crystallite size has been explored in earlier work showing that a decrease in size leads to an increase in the removal capacity and a decrease

in the sorption rate parameter.[7] It was demonstrated that the lower sorption rates in smaller crystals leads to extended kinetic regimes allowing for higher conversion.[6] These previous studies also demonstrated that the average kinetics and capacities determined from a small number of particles using synchrotron-based techniques (i.e., 1 mm x 3 mm beam window for in-situ bulk XAS and 10-20 μm diameter particles for transmission X-ray microscopy[6]) are similar to those deduced from the breakthrough curves of a 0.3 mL fixed beds. This work focuses on the effect of temperature on kinetics and conversion to study the relationship between determining capacities and kinetics using different techniques (i.e., fixed beds and *in-situ* XAS at the Cu and S K-edges).

The fixed bed sorption experiments yielded H_2S concentration breakthrough curves (**Figure S18**) from which the sorption capacities and linear driving force rate parameters can be estimated. A linear driving force model that is zero order in H_2S concentration (see Section 2.3.1 of the SI) describes the breakthrough curves at 323 K, however, at 353 and 383 K, a model that is first order in H_2S concentration describes the curves.[36] The values of rate parameter and conversion of CuO are summarized in **Table S3**. The results show a consistent increase in conversion with an increase in temperature, with complete conversion achieved at 383 K. Moreover, the sorption rate parameter increased following an Arrhenius law relationship with an apparent activation energy of 23.5 kJ mol^{-1}. In our previous study,[6] we demonstrated that bulk mass transfer and macropore diffusion are negligible for pellet sizes of ~75 μm and flowrates of 90 cm^3(STP) min^{-1}. Under these conditions, reaction rate parameters account for reaction-diffusion phenomena in particles with less than ~10 μm diameters (as identified by Transmission X-ray Microscopy).[6] Thus, temperature effects on both reaction and diffusion are likely reflected in this measured activation energy, however, determining the rate of growth of the product layers is required to quantify the relative contributions of diffusion and reaction to the sorption rate, a task that is beyond the scope of the

experiments presented herein. Nonetheless, the rate parameters and activation energy can be useful for semi-quantitative comparison with *in-situ* XAS results.

These *in-situ* XAS experiments (**see Figures S20-S22**) were performed for the same sample (CuO-1) and conditions (1000 ppm-vol H_2S/He at 323, 353 and 383 K) as the fixed bed experiments. At the Cu K-edge, linear combination fitting (LCF) was used to determine the CuO/CuS ratio at every scan-time point, where the spectra of CuS and fresh CuO-1 were used as fitting references. At S K-edge, the edge steps of the spectra were correlated to the extent of conversion, where the saturation edge step for 383 K (complete conversion) was used as a scaling factor. The contribution of H_2S gas was subtracted from spectra for accurate CuS quantification. **Figure S19** presents the conversion curves for these runs, which were analyzed using the random pore model (RPM).[37] Similar to the fixed bed experiments, conversion increased with temperature, and complete conversion was achieved at 383 K. Conversion estimates based on Cu and S K-edge XAS data were similar to conversions measured from fixed beds after similar time of exposure to H_2S on stream (**Table S3**).

The rate parameters and effective diffusivities determined from Cu and S K-edge experiments are summarized in **Table S3**. The 95% confidence intervals for the rate parameters are larger (>20% of the parameter value) than those for the diffusivities (less than 10% of the parameter value), which results from shorter kinetic regimes (i.e., few data points) compared to diffusion controlled regimes. Comparisons of the effective diffusivity values are within the same order of magnitude for both edges, and the activation energies determined from the two experiments conducted at the two edges are within 25% agreement (and less than a factor of 2 larger than the activation energy determined from the fixed bed studies). Thus, we conclude (similar to our previous work) that the kinetic information derived from our *in-situ* XAS experiments is

representative of the kinetics derived from analysis of fixed bed breakthrough curves and is suitable for interpretation of the phenomena that occurs during reaction H_2S sorption.

3.3 Speciation of sulfidation products

The conversion of CuO to CuS is incomplete for all of the sorbents at 1000 ppm-vol H_2S and 298 K (see **Table 1)**. The conversion ranges from a high of 44% for CuO-1 to a low of 3% for CuO-5. This makes the speciation of the sulfidation products somewhat challenging as there is a mixture of species present. However, using a combination of S K-edge XANES, Cu K-edge XANES and EXAFS, and XRD on these spent samples, it is possible to identify the sulfide copper species that are formed. These experiments focused on exploring the effect of crystallite size of the CuO starting material and the effect of temperature on the formed copper sulfide species.

Figure S5 presents the XRD patterns of the CuO sorbents after reaction in fixed bed experiments at 1000 ppm-vol H_2S 298 K, and 1 atm. For all samples, a peak at $2\theta = 48°$ is observed in the pattern of the spent samples, which corresponds to the (110) plane of hexagonal copper (II) sulfide (ICSD 16025). Nevertheless, the low conversion (3-28% as summarized in **Table 1**) along with the overlap of XRD patterns of most sulfides (**Figure 5**) suggests that XRD alone is insufficient in determining the speciation of the formed sulfides. Furthermore, **Figure 6** shows the XRD patterns of spent CuO-1 samples following sulfidation at 323 K, 353 K and 383 K. The patterns show significant broadening of the monoclinic CuO peaks and a consistent increase in the intensity of the $2\theta = 48°$ peak with temperature increase. This is consistent with the increase in conversion with temperature observed in the fixed bed experiments (54-100% for 323-383 K). We note that the conversion of CuO-1 at 383 K is 100% (see **Table S3** and discussion in Section 3.2). While the XRD results for both sets of samples suggest the formation of CuS (covellite), they are insufficient to conclusively identify specific CuS phases and whether any distortions are present.

Mineral name	Composition	Crystal System	Cu oxidation states	S oxidation states
Low-chalcocite	Cu_2S	Monoclinic	0, 1	-2
High-chalcocite	Cu_2S	Hexagonal	0, 1	-2
Djurleite	$Cu_{1.94}S$	Monoclinic	1.03	-2
Anilite	$Cu_{1.75}S$	Orthorhombic	0, 1	-2, 0
Geerite	$Cu_{1.6}S$	Cubic	1.25	-2
Roxbyite	$Cu_{1.81}S$	Triclinic	1	-2
Covellite	CuS	Orthorhombic	1, 2	-1, -2

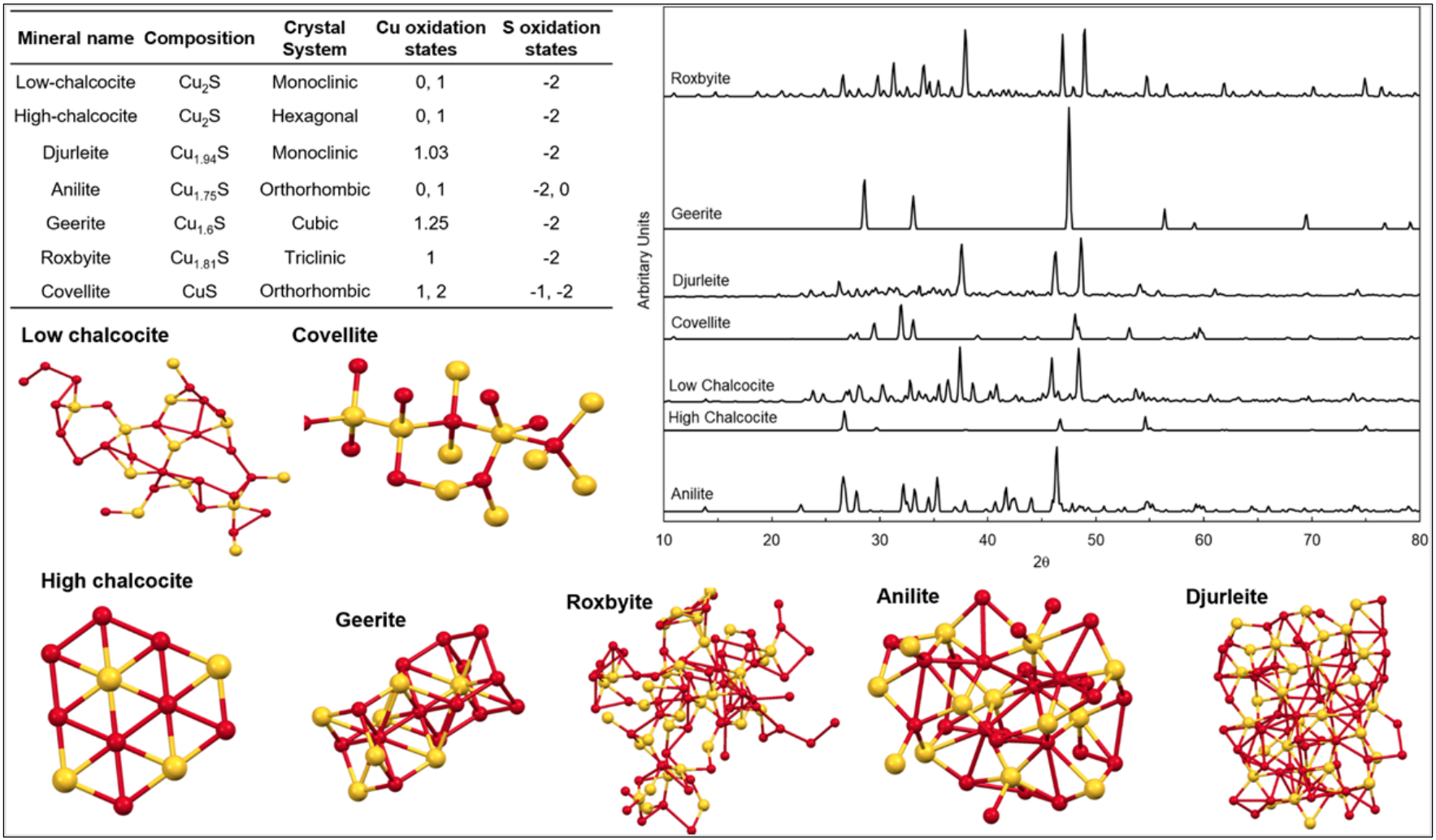

Figure 5. Crystal structures, compositions, oxidation states of Cu and S, and X-ray diffraction patterns for low-chalcocite, high-chalcocite, Djurleite,[38] Anilite,[39] Geerite,[40] Roxbyite,[41] and Covellite.[9] Red spheres represent Cu while yellow spheres represent S. The structures are produced using Mercury 3.8 structural visualization application.[42]

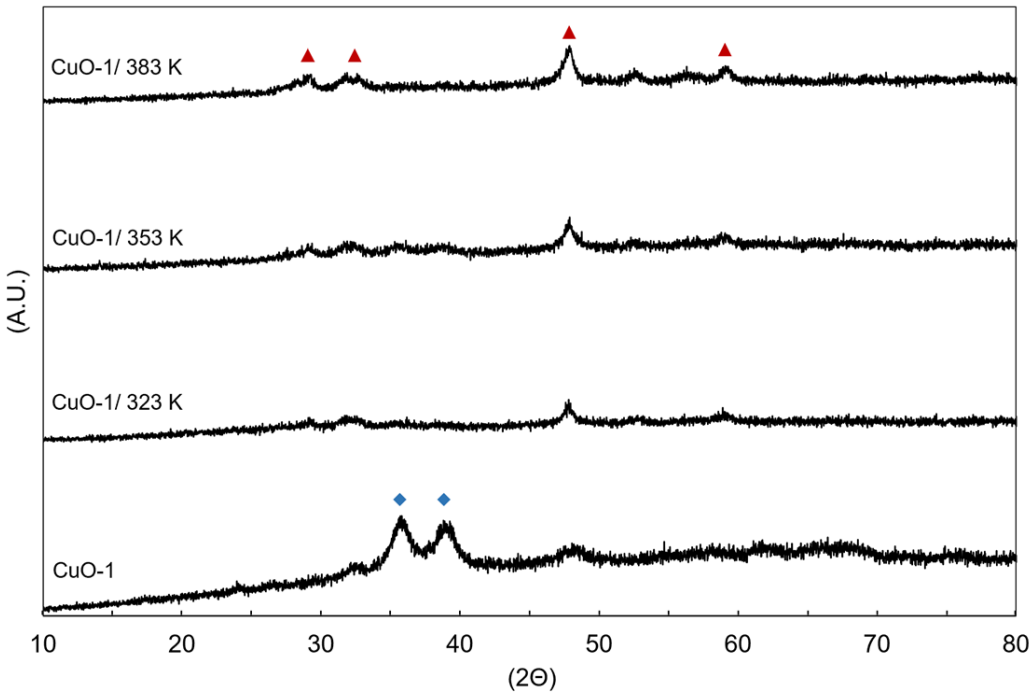

Figure 6. Diffraction patterns of fresh CuO-1 sorbent and spent samples for runs at 323, 353, and 383 K (using 1000 ppm-vol H_2S/N_2 and 90 cm^3(STP) min^{-1}). The XRD of spent samples are collected at 298 K and 1 atm after sulfidation at elevated temperatures. Blue diamonds correspond to characteristic CuO peaks and red triangles correspond to characteristic CuS peaks.

Since different $Cu_{2-x}S$ structures have different electronic and coordination environments of the S and Cu atoms, XANES provides insight into the type of species that is formed. **Figure 7** shows the S K-edge XANES of the spent CuO-1 sample at 323 K, 353 K and 383 K, and CuO-2 and CuO-3 spent at 298 K. Three main observations can be made from this figure: (1) The white line amplitude (peak a) decreases with a decrease in crystallite size, (2) the white line is shifted to lower energy for spent samples at elevated temperatures (353 K and 383 K), and (3) a small pre-edge peak (peak b) is present only at elevated temperatures (353 K and 383 K). The first observation aligns with the discussion of the relationship between crystallite size and white line intensity in the fresh Cu K-edge XANES. The two other observations provide an evidence for the formation of different $Cu_{2-x}S$ species at elevated temperature.

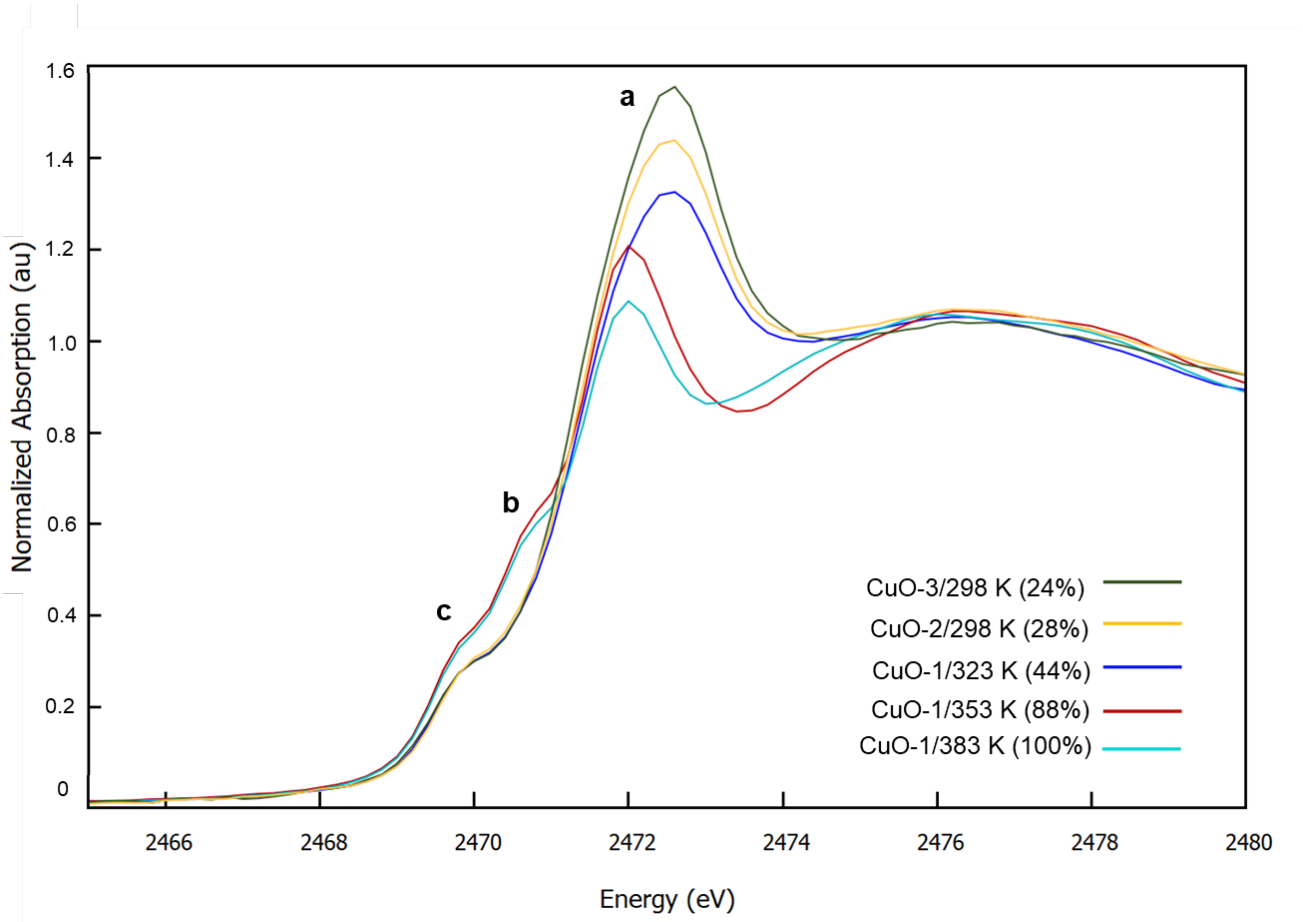

Figure 7. Normalized S K-edge XANES spectra for samples CuO-2 and CuO-3 after reaction at 298 K and CuO-1 after reaction at 323, 353, and 383 K (1000 ppm-vol H_2S/He, 298 K and 1 atm). The scans were collected under flowing He. Experimental conversion of each sample is indicated in the figure legend.

In the S K-edge XANES of the reference covellite (CuS, **Figure 8)**, there are two characteristic pre-edge features, denoted as (b) and (c). These features have previously been assigned to a S^{2-} 1s → Cu^{2+} $3d^9$ transition (2469.9 eV) and a S_2^{2-} 1s → Cu^{2+} $3d^9$ transition (2470.7 eV).[11] It is apparent from the spectra shown in **Figure 8** that in the spent CuO-1 samples at 383 K, both pre-edge peaks are present, but the second peak (b) is absent in the spectra collected on the spent sample at 323 K. (The conversion of CuO-1 at 383 K is 100%, **Table 2**). This difference is further highlighted by the second derivative plots of these spectra (inset of **Figure 8**). The white line (peak a) is assigned to a S_2^{2-} 1s → 3p transition,[11] confirming the presence of S_2^{2-} in all spent samples. Thus,

rather than indicating the absence of disulfide ions, the absence of peak (b) in spent samples at low temperatures (298 and 353 K) indicates that the geometry of the S_2^{2-} in these samples differs from that of S_2^{2-} in bulk covellite (CuS). The pre-edge feature (peak b) is dipole forbidden and quadrupole allowed, and thus, it is present as a weak transition. When this feature is additionally forbidden by symmetry or spin inversion selection rules, it will be so weak that it will no longer be distinguishable from the background. Thus, the transition S_2^{2-} 1s → Cu^{2+} $3d^9$ must also be forbidden by symmetry selection rules for the CuO-1 samples after reaction at 298 and 353 K.

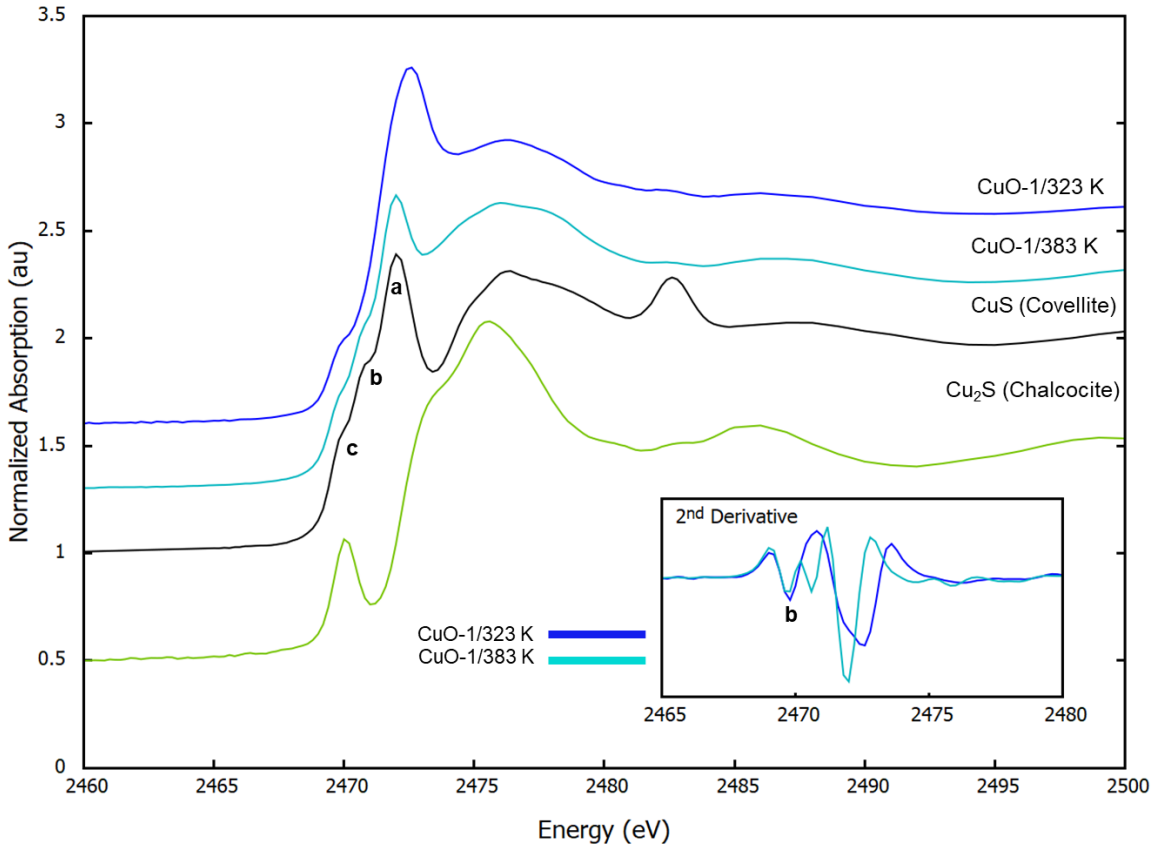

Figure 8. Normalized S K-edge XANES spectra for CuO-1 spent at 323 K and 383 K, and two copper sulfide references (CuS and Cu_2S). The spectra are offset for clarity. The inset shows the second derivative spectra of the spent samples highlighting the absence of peak b (S_2^{2-} 1s → Cu^{2+} $3d^9$) in the sulfided sample at 323 K.

To further explore whether the blue shift (shift to higher energy) of white line is characteristic only of spent samples at lower temperatures, *in-situ* S K-edge XANES spectra of CuO-1 sulfidation at elevated temperatures (353 K and 383 K) are inspected. Interestingly, the CuS species formed in the beginning of the sulfidation process at elevated temperatures matches those in spent samples at low temperatures (See **Figure 9** for 353 K and **Figure S22** for 383 K). **Figure 9** shows the move towards a dampened white line at lower energy, and the emergence of peak b as the reaction progresses at 353 K. Similar behavior is observed at 383 K (**Figure S22**) where the early spectrum, at low conversion, does not show the presence of peak b. This suggests that the formation of this distorted CuS is independent of temperature and its presence is primarily dependent on the total conversion of CuO to CuS. Thus, because the sulfidation begins at interfaces (both the solid-gas interface and crystallite interfaces in the bulk), we suggest that it is at these interfaces that a geometrically distorted CuS structure is formed. As conversion proceeds, the intensity of peak b at 2470.7 eV (associated with the spectral features of bulk covellite) also increases, indicating the formation of bulk CuS away from the reaction interfaces.

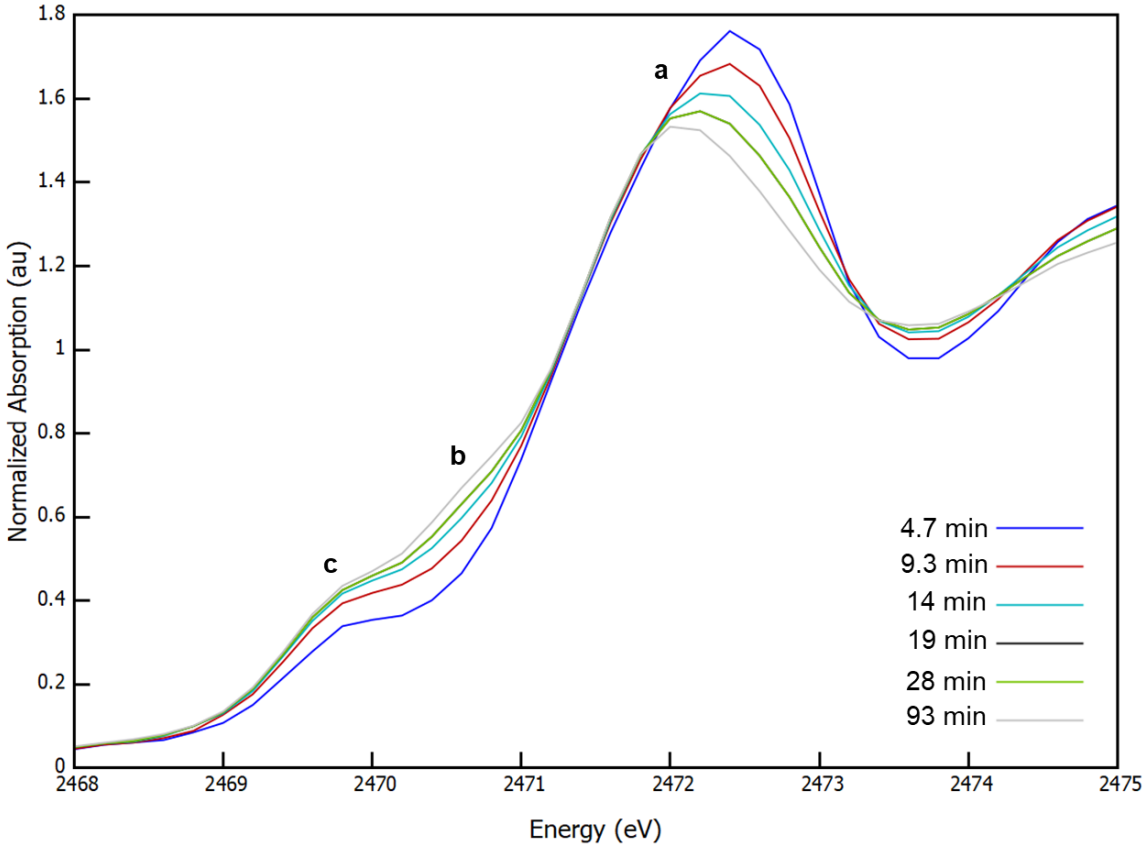

Figure 9. Normalized *in-situ* S K-edge XANES spectra for sample CuO-1 during sulfidation at 353 K, 1000 ppm-vol H_2S/He and 1 atm.

Concurrent with the growth of peak b, is the red shift (lower energy) of the white line observed at the latter stages of the sulfidation process at elevated temperatures. This peak is associated with a S_2^{2-} 1s → 3p transition[15] and it results from the hole character in the S_2^{2-} 3p orbitals due to the delocalization of these orbitals onto the electron deficient metal center. The more electron-deficient metal centers are, the easier it will mix with the 3p orbitals of S_2^{2-}. Thus, small shifts in the energy of this peak can indicate the oxidation state of the metal center itself.[11] In other words, the environment of S_2^{2-} in spent samples at low temperatures is more electropositive than that of S_2^{2-} in bulk covellite. This further supports our theory of distorted CuS structure at the interface of CuO. The higher energy contribution of this peak, in the interfacial region, is because of the Cu^{2+}

centers that are bonded to both O^{2-} and S_2^{2-} ligands. These centers are more electron deficient than Cu^{+}/Cu^{2+} centers in bulk covellite which are only bound to S^{2-} and S_2^{2-}. It is these same S_2-Cu-O centers which are responsible for the strained geometry that causes the disappearance of the 2470.7 eV peak.

3.4 Impact of CuS structure on reaction mechanism

Computational simulations using Density Functional Theory on CuO surfaces show that sulfur exhibits a tendency towards forming S-S bonds at the surface. DFT studies carried out by our group on CuO (111) and ($\bar{1}$11) surfaces, show that, upon dissociative adsorption of H_2S molecules on CuO surfaces (which results in CuO sulfidation and formation of water), sulfur atoms progressively replace oxygen atoms.[43] The net Gibbs free energies for the reaction of CuO (111) / ($\bar{1}$11) surfaces with a H_2S molecule is -106 kJ mol^{-1} and -93 kJ mol^{-1}, respectively, when involving the exchange of O_{3c} atoms with sulfur atoms, and -52 kJ mol^{-1} and -8 kJ mol^{-1} if H_2S reacts with O_{4c} atoms, although the latter values get more favorable if O_{3c} atoms have already been exchanged with S atoms, making ΔG then -101 and -75 kJ mol^{-1}, respectively.

As the reaction progresses and more H_2S is adsorbed (thus releasing H_2O), the sulfur coverage on the oxide surface increases, at which point close sulfur atoms start interacting among them via bonding, which results in sulfur dimers appearing on the surface. To this regard, we have found that the formation of S_2 dimers from adjacent sulfur atoms is thermodynamically favorable, with a calculated Gibbs free energy of reaction of ΔG=-47 kJ mol^{-1}. Adsorbed S atoms on the surface tend to form disulfide bonds, as depicted in **Figure 10**. In this example, one S atom three-fold coordinated (S_{3c}) to three copper atoms approaches another S_{3c} atom, initially at 3 Å of distance. The first S atom (left one in **Figure 10**) breaks one Cu-S bond and gets bonded to the other S atom (right one in **Figure 10**), remaining three-fold coordinated (to two underneath Cu atoms and one

S atom), whereas the second S atom gets a four-fold coordination (to three underneath Cu atoms and one S atom). The newly formed S-S bond has a length of 2.104 Å (for reference, the experimentally measured S-S distance in covellite is 2.071 Å).[44] The fact that, upon increasing sulfur coverage (i.e. as reaction progresses), the S atoms tend to interact among themselves to form S_2 dimer units is in agreement with our experiments showing the presence of S_2-like units during sulfidation of CuO samples. These computational results support the presence of S_2-like units as sulfidation occurs, showing that their formation at the molecular level is thermodynamically favorable.

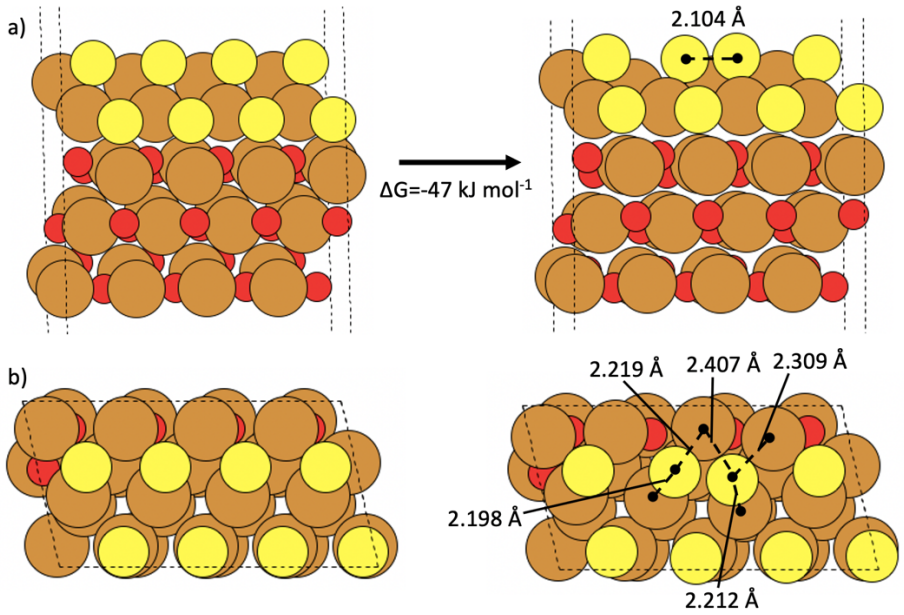

Figure 10. Formation of a S_2 dimer upon S-S bonding by two S adatoms on a sulfided CuO (111) surface (Local minima, no transition state is shown). a) Side view showing the S-S bond length b) Top view showing the Cu-S distances of coordinated Cu atoms to the S_2 unit.

Additionally, reaction pathways for H_2S adsorption on the CuO ($\bar{1}11$) surface show that intermediate structures featuring disulfide bond formation are more favorable than equivalent counterparts without the presence of such bonds. This is exemplified in two pathways, the first on

a bare CuO ($\bar{1}11$) surface where multiple H_2S molecules participate in the reaction and the second one on a partially sulfided CuO ($\bar{1}11$) surface where only one H_2S molecule is involved.

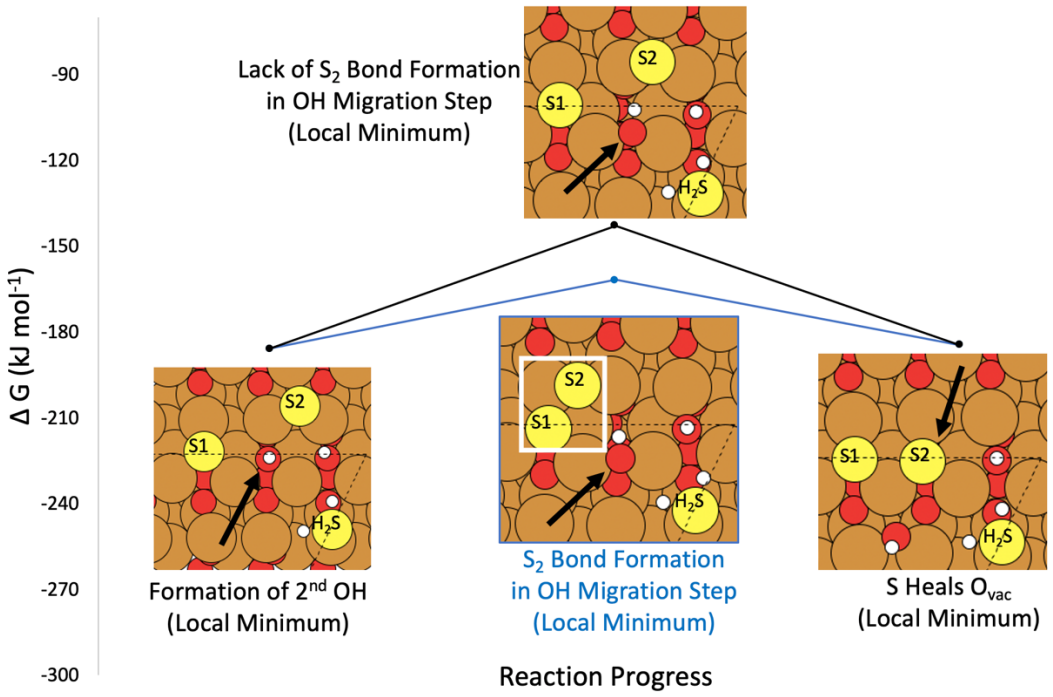

Figure 11. Local minima along part of the reaction pathway on a bare CuO ($\bar{1}11$) surface showing that disulfide bond formation (white box) lowers the reaction free energy, facilitating OH migration. The black arrows on the left and center show the OH group that migrates. In the right the black arrow shows the O_{vac} healed by the S atom. These elementary steps are part of the reaction pathway in which H_2S molecules are adsorbed on CuO surfaces producing at the end sulfided surfaces and H_2O.

In the first case, disulfide bond formation stabilizes the intermediate structure in a step that requires migration of a hydroxyl group, as shown in **Figure 11**. Only the part of the reaction involving hydroxyl migration is shown, with the case featuring disulfide formation in blue, and the case that does not in black. This is an energetically costly process since the hydroxyl is displaced from its equilibrium position on the lattice to a metastable position. However, with favorable sulfur-sulfur interaction, this migration step requires only +24 kJ mol^{-1}, compared to +43 kJ mol^{-1} in the absence of S-S pair. The results highlight that disulfide bond formation is a favorable interaction that facilitates the migration of the OH group.

In the second case, a partially sulfided CuO ($\bar{1}11$) surface is used to simulate the surface in later stages of the reaction, where disulfide bond formation lowers the energy of the structure for the elementary steps involving the formation of a second surface hydroxyl and the subsequent hydroxyl migration. Two S-S bonds preferentially form (blue line for the energy and blue labels for the B and C structures in **Figure 12**). In addition, the presence of a second disulfide bond makes the otherwise endothermic hydroxyl migration step exothermic (from B to C in **Figure 12**), a step which is necessary for water formation. Observation of disulfide bond formation in energy minimization calculations for proposed elementary steps of reaction suggests that disulfide bond formation is favorable during the reactive sorption of H_2S on CuO. These results further support our claim of the dominant presence of the disulfide ions on the surface of CuO crystallites which contributes significantly to the XANES signal at lower conversions.

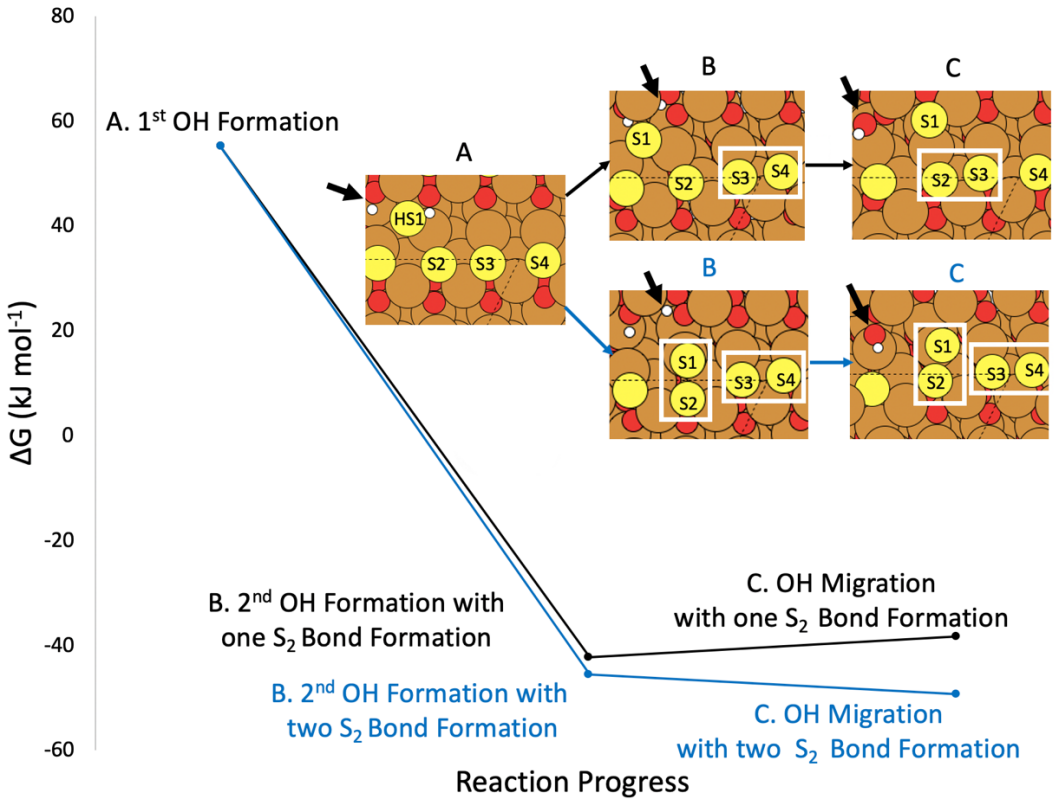

Figure 12. Local minima along part of the reaction pathway on a partially sulfided CuO ($\bar{1}11$) surface where one H_2S molecules participate in reaction, showing the formation of a disulfide

bond (white boxes) and its assistance on the further migration of a surface OH group (from step B to C). Black arrow on A shows the just formed OH from H_2S deprotonation. Black arrows on B show the second OH formed HS deprotonation. Black arrows on C show the migrated OH (the second OH is not shown. It is located outside the snapshot and it is not relevant for the process intended to be shown here.).

Finally, XANES spectra taken at the Cu K-edge of the spent samples (**Figure 13A**) show that as temperature of sulfidation increases from 323 K to 383 K, the features of the CuO starting material, most notably the intense white line at 8998 eV, fade while the features of the covellite form of CuS grow in. Using tenorite (CuO) and covellite (CuS) standards as the basis set, linear combination analysis was performed to determine the degree of sulfidation in these materials. The results are shown in **Table S3**, showing a clear increase in total conversion of CuO to CuS as a function of temperature, with 100% conversion at 383 K. In all spectra, there is a peak around 8978-8979 eV (highlighted by first derivative plot in **Figure 13B**). This peak is only present in compounds containing Cu^{2+} and is absent in the Cu_2S standard (yellow trace), as it results from a Cu^{2+} 1s $\rightarrow$ $3d^9$ transition.[11] Because this peak is forbidden by dipole selection rules, it is much weaker in systems with centrosymmetric ligands (as is the case of CuO) due to decreased p/d orbital hybridization. However, the presence of this peak in spent samples agrees with previous studies of CuS in the covellite structure.[10] Further evidence that Cu^{2+} is present in spent samples can be readily seen when comparing the first derivative of the XANES region (**Figure 13B**) for these materials. The sample sulfided at 323 K shows a weak pre-edge feature at 8979 eV, both because the material only contains 40% CuS, and because much of the CuS that forms is in a strained geometry. However, the strong single peak at 8980 eV from the Cu_2S standard is completely absent in the 323 K spent sample, indicating the lack of the formation of a Cu^{+}-S^{-2} species in this reaction.

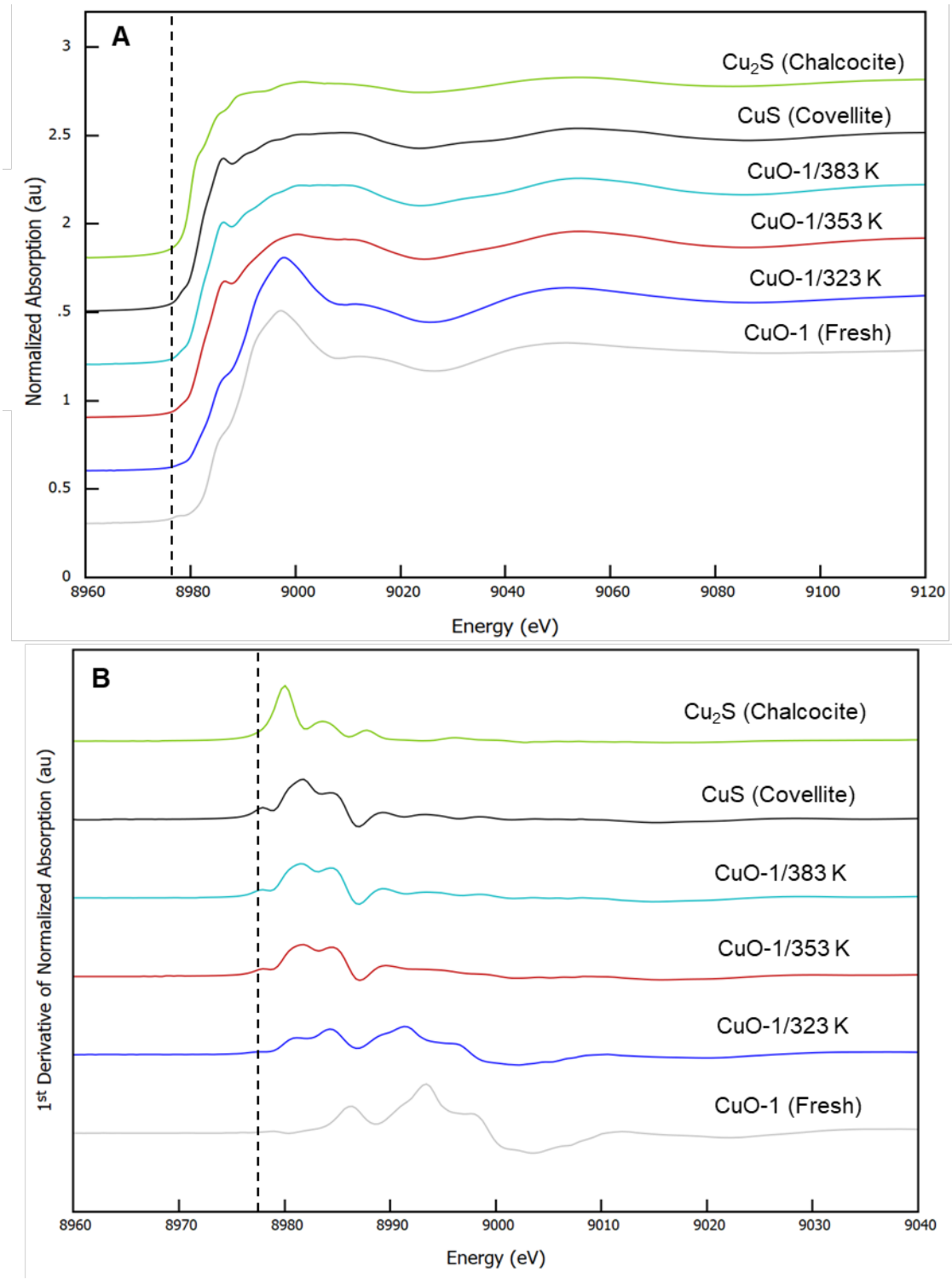

Figure 13. A) Normalized Cu K-edge XANES spectra for fresh CuO-1 sample, spent CuO-1 samples at 323, 353, and 383 K (1000 ppm-vol H_2S/He), and two copper sulfide references (CuS and Cu_2S). B) First derivative spectra of A highlighting the pre-edge feature (dashed line) associated with Cu^{2+} 1s → $3d^9$ transition. Spectra offset for clarity.

Furthermore, the structure of the spent CuO species were analyzed by fitting of the EXAFS region of the Cu K-edge (**Table S2** and **Figures S12-15**). By fixing the Cu-O contributions to the spectra and fitting the Cu-S scattering paths, it can be seen that covellite is a good fit for the spent material at higher conversions (353 and 383 K). At lower conversion, the Cu-S bond distance is appreciably longer (2.30 ± 0.02 Å at 323 K versus 2.26 ± 0.01 Å in covellite reference and sample spent at 383 K). In complement to the results at the S K-edge, this indicates that while the Cu is in a similar oxidation state to that in covellite at lower conversions, a strained geometry is generated by the initial sulfidation of the material. Finally, the coordination numbers of the Cu-S paths, derived from EXAFS models in the spent samples, were consistent with the change in conversion as temperature increased: 1.5 ± 0.5, 3.3 ± 0.1 and 3.4 ± 0.4 at 323 K, 353 K, and 383 K, respectively. These compare with 3.67 coordination in the averaged CuS model.

4. Conclusion

In conclusion, this study sheds light on the sulfidation mechanism of CuO sorbents during the uptake of H_2S. In particular, data are presented highlighting a unique structure at the interfacial CuO-CuS area which, consequently, unravels mechanistic details of the sulfidation process. S K-edge XANES showed evidence of S_2^{2-}, characteristic of CuS, for all spent samples, with a geometrically strained and more electropositive S_2^{2-} form at lower conversions (Spent samples at 298 K and 323 K and early *in-situ* sulfidation spectra of 353 K and 383 K). These differences are because the initially formed disulfide groups are bonded to Cu^{2+} which are bonded to O^{2-} in bulk CuO, as compared to S_2^{2-} in bulk covellite which are connected to Cu^{+}/Cu^{2+} that are bound to S^{2-} and S_2^{2}. The DFT simulations of CuO sulfidation paths (non-sulfided and partially sulfided (111) and ($\bar{1}$11) surfaces), suggest that the formation of disulfide ion is, indeed, thermodynamically favorable in the initial sulfidation stages which aligns with our findings from S K-edge XANES.

Finally, the Cu K-edge EXAFS fits of the sulfided samples show longer Cu-S scattering paths at lower conversions which, again, supports the strained interfacial geometry theory.

5. Associated content

Details of experimental setups, model derivations, additional characterization results, and reaction kinetics analysis are available in the supporting information for this article via a link at the end of the document.

6. Conflict of Interest

There are no conflicts to declare.

7. Acknowledgements

The authors acknowledge financial support from the Henry Samueli School of Engineering and Applied Sciences and the Office of Equity, Diversity, and Inclusion at UCLA and to the donors of The American Chemical Society Petroleum Research Fund for partial support of this research. Use of the SSRL, SLAC National Accelerator Laboratory, and Co-ACCESS, is supported by the U.S. Department of Energy, Office of Science, Office of Basic Energy Sciences, Chemical Sciences, Geosciences and Biosciences under Contract DE-AC02-76SF00515. Additional funding was provided from the US National Science Foundation grant EEC-1647722 (CISTAR). The authors also acknowledge the contribution of Faisal Alshafei for assistance with SEM imaging and Luke Minardi for assistance with N_2 physisorption measurements.

8. References

(1) Kidnay, A. J.; Parrish, W. *Fundamentals of Natural Gas Processing*; CRC Press: Boca Raton, 2006.
(2) Song, C.; Ma, X. New Design Approaches to Ultra-Clean Diesel Fuels by Deep Desulfurization and Deep Dearomatization. *APCATB Appl. Catal. B Environ.* **2003**, *41* (1), 207–238.
(3) Lindenmann, J.; Matzi, V.; Neuboeck, N.; Ratzenhofer-Komenda, B.; Maier, A.; Smolle-Juettner, F.-M. Severe Hydrogen Sulphide Poisoning Treated with 4-Dimethylaminophenol

and Hyperbaric Oxygen. *Diving Hyperb. Med. J. S. Pac. Underw. Med. Soc.* **2010**, *40*, 213–217.
(4) Stankiewicz, A. Reactive Separations for Process Intensification: An Industrial Perspective. *Chem. Eng. Process. Process Intensif.* **2003**, *42* (3), 137–144.
(5) Sharma, M.; Vyas, R. K.; Singh, K. A Review on Reactive Adsorption for Potential Environmental Applications. *Adsorption* **2013**, *19* (1), 161–188.
(6) Hoffman, A. S.; Azzam, S.; Zhang, K.; Xu, Y.; Liu, Y.; Bare, S. R.; Simonetti, D. A. Direct Observation of the Kinetics of Gas–Solid Reactions Using in Situ Kinetic and Spectroscopic Techniques. *React. Chem. Eng.* **2018**, *3* (5), 668–675. https://doi.org/10.1039/C8RE00020D.
(7) Azzam, S. A.; Alshafei, F. H.; López-Ausens, T.; Ghosh, R.; Biswas, A. N.; Sautet, P.; Prikhodko, S.; Simonetti, D. A. Effects of Morphology and Surface Properties of Copper Oxide on the Removal of Hydrogen Sulfide from Gaseous Streams. *Ind. Eng. Chem. Res.* **2019**, *58* (40), 18836–18847.
(8) Pattrick, R. A. D.; Mosselmans, J. F. W.; Charnock, J. M.; England, K. E. R.; Helz, G. R.; Garner, C. D.; Vaughan, D. J. The Structure of Amorphous Copper Sulfide Precipitates: An X-Ray Absorption Study. *Geochim. Cosmochim. Acta* **1997**, *61* (10), 2023–2036. https://doi.org/10.1016/S0016-7037(97)00061-6.
(9) Fjellvåg, H.; Grønvold, F.; Stølen, S.; Andresen, A.; Müller-Käfer, R. Low-Temperature Structural Distortion in CuS. *Z. Krist. - Z Krist.* **1988**, *184*, 111–121. https://doi.org/10.1524/zkri.1988.184.1-2.111.
(10) Li, D.; Bancroft, G. M.; Kasrai, M.; Fleet, M. E.; Feng, X. H.; Yang, B. X.; Tan, K. H. S K- and L-Edge XANES and Electronic Structure of Some Copper Sulfide Minerals. *Phys. Chem. Miner.* **1994**, *21* (5), 317–324. https://doi.org/10.1007/BF00202096.
(11) Kumar, P.; Nagarajan, R.; Sarangi, R. Quantitative X-Ray Absorption and Emission Spectroscopies: Electronic Structure Elucidation of Cu2S and CuS. *J. Mater. Chem. C* **2013**, *1* (13), 2448. https://doi.org/10.1039/c3tc00639e.
(12) Bare, S.; Ressler, T. Chapter 6 Characterization of Catalysts in Reactive Atmospheres by X-Ray Absorption Spectroscopy. *Adv. Catal. - ADVAN CATAL* **2009**, *52*, 339–465. https://doi.org/10.1016/S0360-0564(08)00006-0.
(13) Koningsberger, D. C.; Prins, R. (eds.). *X-Ray Absorption: Principles, Applications, Techniques of EXAFS, SEXAFS, and XANES*; John Wiley and Sons,New York, NY: United States, 1988.
(14) Kayani, Z. N.; Umer, M.; Riaz, S.; Naseem, S. Characterization of Copper Oxide Nanoparticles Fabricated by the Sol–Gel Method. *J. Electron. Mater.* **2015**, *44* (10), 3704–3709. https://doi.org/10.1007/s11664-015-3867-5.
(15) Bolin, T. B.; Wu, T.; Schweitzer, N.; Lobo-Lapidus, R.; Kropf, A. J.; Wang, H.; Hu, Y.; Miller, J. T.; Heald, S. M. In Situ Intermediate-Energy X-Ray Catalysis Research at the Advanced Photon Source Beamline 9-BM. *Catal. Today* **2013**, *205*, 141–147. https://doi.org/10.1016/j.cattod.2012.09.034.
(16) Ravel, B.; Newville, M. ATHENA, ARTEMIS, HEPHAESTUS: Data Analysis for X-Ray Absorption Spectroscopy Using IFEFFIT. *J. Synchrotron Radiat.* **2005**, *12* (4), 537–541. https://doi.org/10.1107/S0909049505012719.
(17) Inorganic Crystal Structure Database – ICSD | FIZ Karlsruhe https://www.fiz-karlsruhe.de/de/produkte-und-dienstleistungen/inorganic-crystal-structure-database-icsd (accessed Aug 31, 2019).

(18) Kresse, G.; Hafner, J. Ab Initio Molecular-Dynamics Simulation of the Liquid-Metal–Amorphous-Semiconductor Transition in Germanium. *Phys. Rev. B* **1994**, *49* (20), 14251.
(19) Kresse, G.; Hafner, J. Ab Initio Molecular Dynamics for Liquid Metals. *Phys. Rev. B* **1993**, *47* (1), 558.
(20) Kresse, G.; Furthmüller, J. Efficiency of Ab-Initio Total Energy Calculations for Metals and Semiconductors Using a Plane-Wave Basis Set. *Comput. Mater. Sci.* **1996**, *6* (1), 15–50.
(21) Perdew, J. *In Electronic Structure of Solids' 91; Ziesche, P.; Eschrig, H., Eds*; Akademie Verlag: Berlin, 1991.
(22) Perdew, J. P.; Burke, K.; Ernzerhof, M. Generalized Gradient Approximation Made Simple. *Phys. Rev. Lett.* **1996**, *77* (18), 3865.
(23) Anisimov, V. I.; Zaanen, J.; Andersen, O. K. Band Theory and Mott Insulators: Hubbard U Instead of Stoner I. *Phys. Rev. B* **1991**, *44* (3), 943–954. https://doi.org/10.1103/PhysRevB.44.943.
(24) Anisimov, V. I.; Aryasetiawan, F.; Lichtenstein, A. First-Principles Calculations of the Electronic Structure and Spectra of Strongly Correlated Systems: The LDA+ U Method. *J. Phys. Condens. Matter* **1997**, *9* (4), 767.
(25) Wu, D.; Zhang, Q.; Tao, M. LSDA+ U Study of Cupric Oxide: Electronic Structure and Native Point Defects. *Phys. Rev. B* **2006**, *73* (23), 235206.
(26) Dudarev, S. L.; Botton, G. A.; Savrasov, S. Y.; Humphreys, C. J.; Sutton, A. P. Electron-Energy-Loss Spectra and the Structural Stability of Nickel Oxide: An LSDA+ U Study. *Phys. Rev. B* **1998**, *57* (3), 1505.
(27) Mishra, A. K.; Roldan, A.; de Leeuw, N. H. CuO Surfaces and CO2 Activation: A Dispersion-Corrected DFT+U Study. *J. Phys. Chem. C* **2016**, *120* (4), 2198–2214. https://doi.org/10.1021/acs.jpcc.5b10431.
(28) Nolan, M.; Elliott, S. D. The P-Type Conduction Mechanism in Cu 2 O: A First Principles Study. *Phys. Chem. Chem. Phys.* **2006**, *8* (45), 5350–5358.
(29) Yang, B.; Thurston, T.; Tranquada, J.; Shirane, G. Magnetic Neutron Scattering Study of Single-Crystal Cupric Oxide. *Phys. Rev. B* **1989**, *39* (7), 4343.
(30) \AAsbrink, S.; Norrby, L.-J. A Refinement of the Crystal Structure of Copper (II) Oxide with a Discussion of Some Exceptional Esd's. *Acta Crystallogr. B* **1970**, *26* (1), 8–15.
(31) Larsen, A. H.; Mortensen, J. J.; Blomqvist, J.; Castelli, I. E.; Christensen, R.; Du\lak, M.; Friis, J.; Groves, M. N.; Hammer, B.; Hargus, C.; others. The Atomic Simulation Environment—a Python Library for Working with Atoms. *J. Phys. Condens. Matter* **2017**, *29* (27), 273002.
(32) Monkhorst, H. J.; Pack, J. D. Special Points for Brillouin-Zone Integrations. *Phys. Rev. B* **1976**, *13* (12), 5188.
(33) Neugebauer, J.; Scheffler, M. Adsorbate-Substrate and Adsorbate-Adsorbate Interactions of Na and K Adlayers on Al (111). *Phys. Rev. B* **1992**, *46* (24), 16067.
(34) Sharma, A.; Varshney, M.; Park, J.; Ha, T.-K.; Chae, K.-H.; Shin, H.-J. XANES, EXAFS and Photocatalytic Investigations on Copper Oxide Nanoparticles and Nanocomposites. *RSC Adv.* **2015**, *5* (28), 21762–21771.
(35) Marinkovic, N. S.; Sasaki, K.; Adzic, R. R. Determination of Single- and Multi-Component Nanoparticle Sizes by X-Ray Absorption Spectroscopy. *J. Electrochem. Soc.* **2018**, *165* (15), J3222–J3230. https://doi.org/10.1149/2.0281815jes.

(36) Cooper, R. S. Slow Particle Diffusion in Ion Exchange Columns. *Ind. Eng. Chem. Fundam.* **1965**, *4* (3), 308–313. https://doi.org/10.1021/i160015a012.
(37) Bhatia, S. K.; Perlmutter, D. D. A random pore model for fluid-solid reactions: I. Isothermal, kinetic control. *AIChE J.* **1980**, *26* (3), 379–386. https://doi.org/10.1002/aic.690260308.
(38) Evans, H. T. The Crystal Structures of Low Chalcocite and Djurleite. 22.
(39) Koto, K.; Morimoto, N. The Crystal Structure of Anilite. *Acta Crystallogr. B* **1970**, *26* (7), 915–924. https://doi.org/10.1107/S0567740870003370.
(40) R. J. Goble, R. I.; George Robinson. Geerite, Cu (Sub 1.60) S, a New Copper Sulfide from Dekalb Township, New York. *Can. Mineral.* **1980**, *18* (4), 519–523.
(41) Mumme, W. G.; Gable, R. W.; Petricek, V. The Crystal Structure of Roxbyite, Cu58S32. *Can. Mineral.* **2012**, *50* (2), 423–430. https://doi.org/10.3749/canmin.50.2.423.
(42) Mercury - The Cambridge Crystallographic Data Centre (CCDC) https://www.ccdc.cam.ac.uk/solutions/csd-system/components/mercury/ (accessed Oct 17, 2019).
(43) Lopez-Ausens, T.; Chiang, N.; Simonetti, D.; Sautet, P. On the Mechanism of Reactive Sorption of H2S on CuO (111) and (-111) Surfaces: A First-Principles Study. *Be Publ.* **2020**.
(44) Evans, H.; Konnert, J. Crystal Structure Refinement of Covellite. *Am Miner.* **1976**, *61* (9–10), 996–1000.

9. TOC Graphic